

Article

Two-Phase Flow Visualization and Heat Transfer Characteristics Analysis in Ultra-Long Gravity Heat Pipe

Feng Li ^{1,2,3,4}, Juanwen Chen ^{1,2,3,*}, Jiwen Cen ^{1,2,3} , Wenbo Huang ^{1,2,3}, Zhibin Li ^{1,2,3,4}, Qingshan Ma ^{1,2,3,5} and Fangming Jiang ^{1,2,3,*} 

¹ Guangzhou Institute of Energy Conversion, Chinese Academy of Sciences, Guangzhou 510640, China; lifeng@ms.giec.ac.cn (F.L.)

² CAS Key Laboratory of Renewable Energy, Guangzhou 510640, China

³ Guangdong Provincial Key Laboratory of New and Renewable Energy Research and Development, Guangzhou 510640, China

⁴ University of Chinese Academy of Sciences, Beijing 100049, China

⁵ School of Energy Science and Technology, University of Science and Technology of China, Guangzhou 510640, China

* Correspondence: chenjw@ms.giec.ac.cn (J.C.); jiangfm@ms.giec.ac.cn (F.J.)

Abstract: The ultra-long gravity heat pipe has a long heat transfer distance and narrow working fluid flow channel within its tube. Due to these unique design features, the vapor–liquid counter-flow and heat transfer characteristics of these heat pipes are more complex than those found in conventional-size heat pipes. This paper innovatively proposes the design of a segmented visualization window structure of an ultra-long gravity heat pipe, which successfully overcomes the challenge of visualizing the internal flow during operations. A visualization experimental platform, measuring 40 m in height with an inner diameter of 7 mm and the aspect ratio up to 5714, was built to investigate the evolving characteristics of two-phase flows with an increasing heat input and the impact of the phase change flow characteristics on the thermal performance of ultra-long gravity heat pipes. The results obtained can provide guidance for the development of the internal structure of ultra-long gravity heat pipes that are being applied in exploiting geothermal energy. The results show that, at low heat input (200 W, 250 W), there are separate flow paths between the condensate return and the steam, but the high hydrostatic pressure due to the height of the liquid injection results in the presence of an unsaturated working fluid with a higher temperature in the liquid pool area, which has a lower evaporation rate, limiting the heat transfer through the heat pipe. It is found that if increasing the heat input up to 300 W, the evaporative phase change in the heating section becomes intense and stable. At the same time, despite the intermittent formation of liquid columns in the adiabatic section due to the vapor–liquid rolls, which increases the resistance to the vapor–liquid counter-flow, the liquid columns are blocked for a short period of time, and the path of steam rises and the condensate return is smooth, which does not seriously affect the steam condensation and liquid return evaporation. At this point, the overall temperature of the heat pipe is evenly distributed along the tube and the heat transfer performance is optimal. When the heat input further increases (350 W, 400 W), a large amount of condensate is trapped in the upper part of the adiabatic section and the condensing section by long liquid plugs for a long time. At this point, the condensate flow back to the heating section is significantly reduced, and the steam is seriously prevented from entering the condensation section, resulting in a significant increase in the temperature gradient between the lower part of the evaporating section and the upper part of the adiabatic section and deterioration of the heat transfer performance.

Keywords: ultra-long gravity heat pipe; vapor–liquid two-phase flow; phase change heat transfer; geothermal energy; visualization



Citation: Li, F.; Chen, J.; Cen, J.; Huang, W.; Li, Z.; Ma, Q.; Jiang, F. Two-Phase Flow Visualization and Heat Transfer Characteristics Analysis in Ultra-Long Gravity Heat Pipe. *Energies* **2023**, *16*, 4709. <https://doi.org/10.3390/en16124709>

Academic Editor: Dmitry Eskin

Received: 13 May 2023

Revised: 31 May 2023

Accepted: 31 May 2023

Published: 14 June 2023



Copyright: © 2023 by the authors. Licensee MDPI, Basel, Switzerland. This article is an open access article distributed under the terms and conditions of the Creative Commons Attribution (CC BY) license (<https://creativecommons.org/licenses/by/4.0/>).

1. Introduction

Geothermal energy, with its features of vast reserves, sustainable exploitation, and minimal environmental impacts, has become a crucial constituent in the development and utilization of renewable energy. The extraction of geothermal energy using heat pipes has recently received increasing attention [1–7]. Gravity heat pipes are capable of spontaneously conveying the heat from the underground to the surface by means of evaporation and condensation of the working fluid inside the pipes, thus achieving high-efficiency thermal utilization of geothermal energy and yielding superior technical and economic benefits [8,9].

Heat pipes, as a highly efficient heat transfer device, have been widely used in various fields such as energy and chemical industries [10–14]. This includes efficient heat dissipation in data centers [15], solar power utilization [16–18], etc. However, conventional heat pipes usually have a length within 10 m, while gravity heat pipes used for geothermal energy extraction require satisfying the demand of underground heat source depth. As a result, their lengths can range from tens to thousands of meters, with a length-to-diameter ratio much greater than that of conventional heat pipes. In the ultra-long gravity heat pipe, a long-distance vapor–liquid phase change and vapor–liquid counter-current flow are present. However, the empirical formula and parameters of conventional heat pipes are not suitable for ultra-long gravity heat pipes. Liu [19] tested the heat transfer limit of a 48 m long thermosyphon and concluded that the carrying behavior of the two-phase flow led to dry-out of the liquid pool at the bottom of the heating section, resulting in the thermosyphon reaching its heat transfer limit. Hu [20] investigated the heat transfer characteristics of an ultra-long lithium heat pipe through modeling and suggested that the vapor thermal resistance decreases with increased heating power. Moreover, the dry area in the pipe increases with an increase in the length of the adiabatic section at any given vapor temperature. At present, studies have shown that when ultra-long gravity heat pipes operate, problems such as unstable operation due to the instability of two-phase flow and high static water pressure that restricts heat transfer may occur [21–23]. Nevertheless, the current research results on vapor–liquid flow and phase change mechanisms of ultra-long gravity heat pipes mainly rely on reasonable deduction based on temperature and pressure data, and further experimental verification is still required.

The processes of heat and mass transfer are widespread but complex. They exist in the production of fuel cell electrodes [24] as well as in the extraction of natural gas hydrates, oil and gas [25,26]. Visual experimental research is an effective method to gain a deep understanding of these processes, revealing the mechanism of flow and heat transfer in heat pipes. This method is particularly common in the study of heat transfer performance in heat pipe flow. The measurement method of Capacitance void fraction sensors are an advanced means to obtain the distribution of two-phase fluids [27,28]. Due to limited experimental conditions, the visualized research presented in this article was accomplished by recording the flow of two-phase fluid within transparent materials. In this paper, a visualization experimental platform of ultra-long gravity heat pipe with a length of 40 m, an inner diameter of 7 mm, and a length-to-diameter ratio of 5714 was built by implementing a segmented window design to solve the visualization experimental difficulties encountered with ultra-long gravity heat pipes. Experimental observations of the vapor–liquid two-phase operation and heat transfer behavior in different regions of the tube during the operation of an extra-long gravity heat pipe provide insight into the evaporative boiling and condensation heat transfer phenomena. Additionally, the interaction mechanism between the long-distance vapor–liquid counter-flow in the adiabatic section is also revealed, shedding light on the performance of ultra-long gravity heat pipes.

2. Experimental System

2.1. Experimental Setup and Procedure

Due to the large length and high pressure requirements of the pipe body, it is difficult to adopt the full-body visualization design of conventional heat pipes in visual experiments for ultra-long gravity heat pipes [16]. Therefore, in this study, we have designed a segmented

visualization window structure. The main body of the ultra-long gravity heat pipe consisted of a copper tube with a length of 40 m, an outer diameter of 10 mm, an inner diameter of 7 mm, and a length-to-diameter ratio of up to 5714. Three visible windows were set on the copper tube for visualization. The schematic diagram of the experimental system is shown in Figure 1. The heat pipe in the experimental system is mainly divided into three sections: the heating section, adiabatic section, and condensing section. The heating section is 20 m long and is heated by the electric wire wound around the copper tube. A Window I is arranged in the heating section, as shown in Figure 2. The window is 0.25 m long and is constructed by connecting a copper tube and an organic glass tube with two half-cylinders with a diameter of 7 mm machined on copper plate and organic glass plate, respectively, to form a circular channel with a diameter of 7 mm. Silicone gaskets are placed between the copper plate and the organic glass plate to ensure vacuum sealing. The back of the copper plate is grooved to arrange the heating wires. The connection between the copper tube and the window segment is also made by tightening with bolts and silicone gaskets. Considering the restrictions of the experimental site, the position of the lower end of Window I is 3.25 m away from the bottom of the heat pipe. The adiabatic section, which is 15 m long, has Window II and Window III installed at the bottom and top, respectively, each with a length of 0.25 m. The special clamp connecting the copper tubes between them is used to connect with the organic glass tubes with the same inner and outer diameters as the copper tubes. The distances from the lower end of Window II and Window III to the bottom of the heat pipe are 20 m and 34.75 m, respectively. The condensing section is 5 m long and is equipped with a jacket outside the copper tube to allow cooling water to flow upwards and condense the steam and take away the heat. The cooling water flow is controlled by valves and differential flow meters. Except for the window section, the heat pipe is wrapped with a 40 mm thick insulation material to reduce heat loss, and the thermal insulation cotton of the condensing section is wrapped on the outside of the water jacket. At the bottom of the heat pipe, a horizontal 3 mm thin tube is connected to a drain valve for replacing the working fluid, while at the top, a thin tube is connected to the working fluid storage tank and vacuum pump. The valves are installed on the thin tubes to control the channel switch.

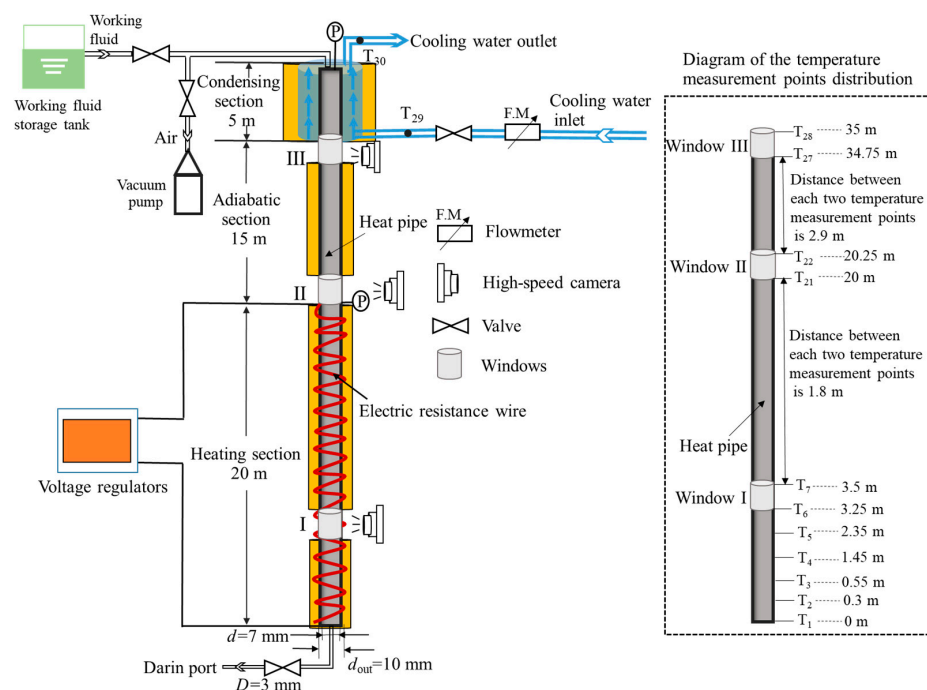


Figure 1. Schematic diagram of the experimental system for visualization of ultra-long gravity heat pipe.

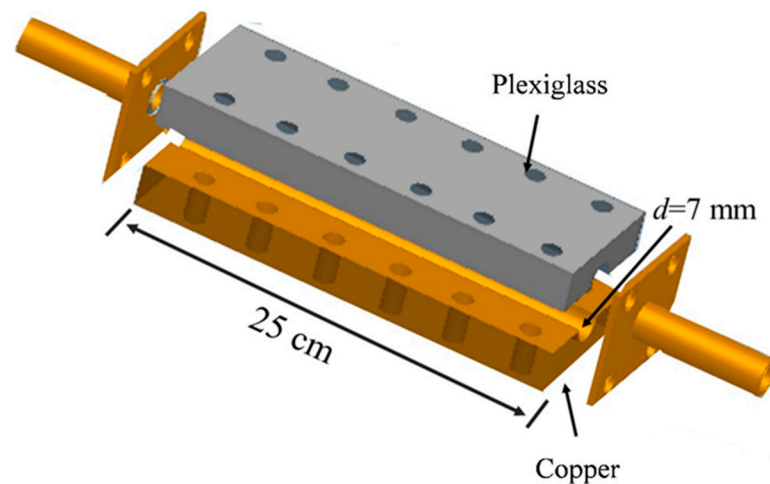


Figure 2. Schematic diagram of the viewport structure of the ultra-long gravity heat pipe heating section.

Pressure sensors are installed at the outlet of the heating section and the top of the heat pipe to monitor the local pressure inside the pipe. The heat pipe surface is equipped with 28 thermocouple temperature measurement points, with 21 measurement points T_1 – T_{21} arranged from the bottom up in the heating section and 7 measurement points T_{22} – T_{28} arranged from the bottom up in the adiabatic section. The distribution of the measurement points is shown in Figure 1. The temperature measurement point at the bottom of the heat pipe is T_1 , and there are measurement points at both ends of the window, which are arranged from the bottom up as T_6 , T_7 , T_{21} , T_{22} , T_{27} , and T_{28} . Temperature measurement points are also evenly distributed between the windows, with T_8 – T_{20} being evenly distributed between T_7 – T_{21} , each measuring point being approximately 1.18 m apart. T_{23} – T_{26} are evenly distributed between T_{22} – T_{27} , with each measuring point being approximately 2.9 m apart. The temperature measurement points at the inlet and outlet of the cooling water are T_{29} and T_{30} , respectively.

Considering that the heat pipe windows have multiple sealing interfaces, the heat pipe must be tested for sealing before each experiment. Before the experiment starts, the heat pipe is evacuated by a vacuum pump until the pressure inside the pipe is below 500 Pa. The pressure inside the pipe is kept for 4 h, and if the pressure increase is less than 100 Pa, the sealing of the heat pipe is considered to meet the requirements for conducting experiments.

At the start of the experiment, the heat pipe was evacuated with a vacuum pump, filled with deionized water as the working fluid, and the cooling water cycle was initiated to adjust the flow rate. According to the research results of Chen et al. [16], the optimal thermal performance of the heat pipe is achieved when the fill height (FH) is 6 m. Therefore, in this study, a flow rate of 3 mL/s of cooling water and a fill height of 6 m were employed as the preset conditions. The heat pipe was heated by adjusting the voltage regulator to investigate the thermal performance and two-phase flow characteristics of the heat pipe as the heating power varied. The temperature of each measurement point during the operation of the heat pipe was recorded and saved in real-time using a data acquisition system. Furthermore, the changes in the two-phase flow of the working fluid in the viewing window were captured by a high-speed camera during the operation of the heat pipe. To ensure that the heat pipe reaches a steady-state, each experimental condition was sustained for at least 2.5 h.

2.2. Uncertainty Analysis

Uncertainty in the current experiment mainly arises from several aspects:

- (1) Temperature measurement is performed using a Pt100 platinum resistance thermometer with a temperature range from 0 to 300 °C, with a maximum allowable mea-

surement error of 0.3%. The uncertainty of the temperature measurement using a resistance thermometer is $U_T = 0.3\%$.

- (2) Pressure monitoring is accomplished using a ceramic capacitive pressure transmitter with an accuracy of 0.1% and a measuring range from 0 to 200 kPa. The uncertainty of the pressure measurement is $U_p = 0.1\%$.
- (3) The heating power Q_{in} of the electric heating wire in the experiment is measured via a wattmeter, with an uncertainty of 0.4%; thus, the uncertainty of heating power $U_{Q_{in}}$ is 0.4%. Since the temperature of the heat pipe is higher than the ambient temperature during operation and heat is dissipated to the environment, the actual heat input to the heat pipe is the difference between the heating power of the electric heating wire and the heat dissipation of the heat pipe. The heating power mentioned in this article refers to the heating power of the electric heating wire.
- (4) The cooling water flow rate V is read from a flow meter, with an uncertainty of $U_V = 0.2\%$.
- (5) The heat transfer of the heat pipe is indirectly calculated using the heat received by the cooling water, which can be calculated based on the inlet and outlet temperatures of the cooling water, and the heat transfer is $Q_{out} = \rho c_p V(T_{30} - T_{29})$, where c_p and ρ are the specific heat capacity and density of the cooling water, respectively. The relative uncertainty of the heat quantity is $U_{Q_{out}} = [(U_T)^2 + (U_V)^2]^{-1/2} = 0.361\%$.

3. Result Analysis

3.1. The Heat Transfer Performance of Heat Pipe

Figure 3 shows the variations of the heat transfer amount (heat absorbed by cooling water) and the heat transfer rate (ratio of heat absorbed by cooling water to heating power) with increasing the heating power for the ultra-long gravity heat pipe. As shown in Figure 3, both the heat transfer amount and the heat transfer rate exhibit an increasing–decreasing trend with increasing the heating power. The results show that the highest thermal performance of the heat pipe is obtained at a heating power of 300 W with a corresponding heat transfer rate of 31%.

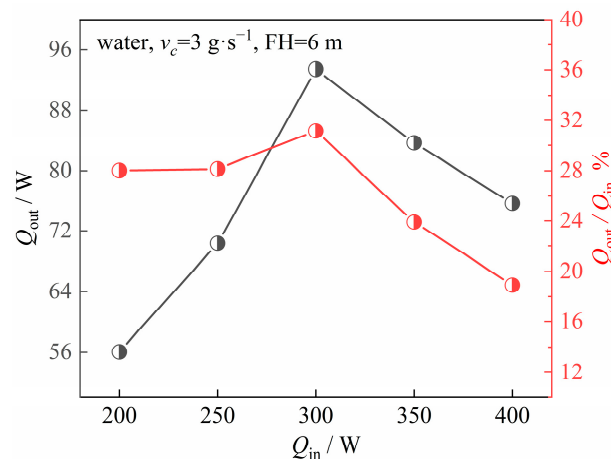


Figure 3. Heat transfer performance of ultra-long gravity heat pipe at different Q_{in} .

Figure 4 provides an overview of the average temperature changes along the height of the heat pipe during stable operation for the different levels of heating power. It can be seen from the figure that the overall temperature of the heat pipe increases as the heating power increases. The uniformity of the heat pipe temperature is an important characteristic of its heat transfer performance, as can be evidenced by the temperature changes along the pipe during stable operation in Figure 4. Under the working condition of 300 W, the degree of temperature uniformity of the heat pipe is higher than those of low heating power (200 W, 250 W) and high heating power (350 W, 400 W) conditions. In the case of low heating power (200 W, 250 W), the temperatures of each measuring point undergo

faint fluctuations around 40 °C and 50 °C above 5 m of the heating section. Moreover, a high-temperature section below 5 m of the heat pipe was observed, as shown in area “a” in Figure 4, where the highest temperature is up to 68 °C. The temperature of the measuring points in the adiabatic section gradually declines with the height. Under moderate heating power (300 W), the high-temperature section at the bottom of the heat pipe disappears, and the temperature of the measuring points in the heating section fluctuates at about 62 °C. The temperature of the measuring points in the adiabatic section slowly decreases with increasing the height, and the optimal uniformity of the heat pipe temperature is achieved at $Q_{in} = 300$ W, characterized by a temperature gradient of -0.6 °C/m. As Q_{in} increases to 350 W, the temperature of the measuring points located below the end of the adiabatic section fluctuates at around 70 °C, with good uniformity of the heat pipe temperature. However, the temperature at the end of the adiabatic section drops sharply, as shown in area “c” in Figure 4. The temperature gradient in this region is -2.54 °C/m, which increases compared to a heating rate of 300 W (-1.8 °C/m) and is also significantly higher than the temperature gradient in the middle and lower part of the adiabatic section (-0.96 °C/m). As the heating capacity continues to increase to 400 W, a significant increase in temperature occurs in the lower part of the heating section of the heat pipe, as presented in area “b” in Figure 4, with a maximum temperature of 120 °C. Meanwhile, the temperature gradient in the upper part of the adiabatic section is further increased, and the region with large temperature difference is significantly expanded downward compared to the 350 W condition, as shown in area c of Figure 4, where the temperature gradient is -3.81 °C/m.

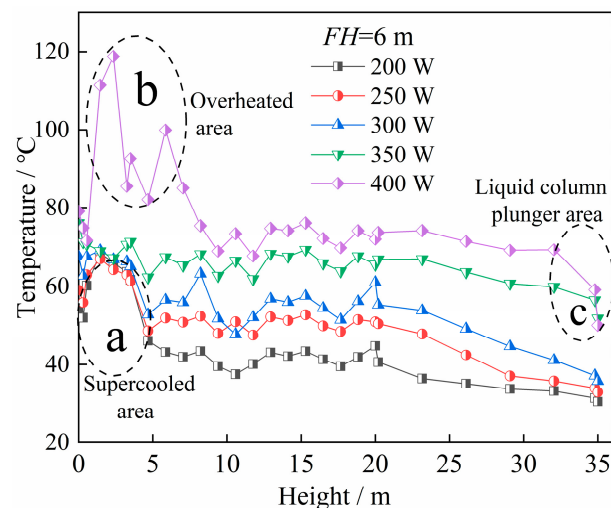


Figure 4. Temperature distribution along the tube when the heat pipe operates stably.

In the following section, the two-phase flow phenomenon in the tube is visualized and analyzed in terms of the boiling behavior of the working fluid in the heating section (Window I), the behavior of the gas–liquid two-phase flow at the inlet of the adiabatic section (Window II) and the outlet of the adiabatic section (Window III).

3.2. Boiling Behavior of the Working Fluid in the Lower Part of the Heating Section

Figure 5 shows the boiling behavior of the working fluid in Window I under stable operation of an ultra-long gravity heat pipe at different heating powers. Meanwhile, Figure 6 provides insight into the temporal evolution of the vapor volume fraction (defined as the ratio of vapor volume to window volume) in Window I from onset nucleation at different heating powers.

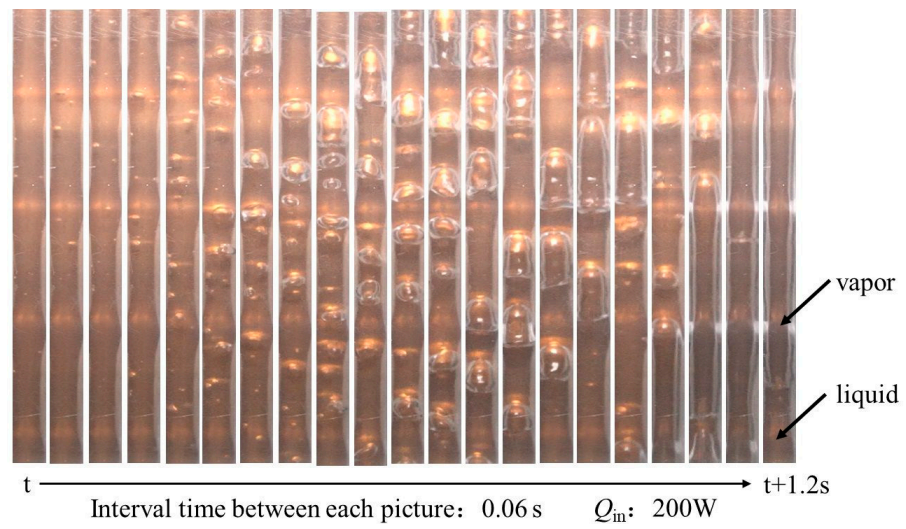
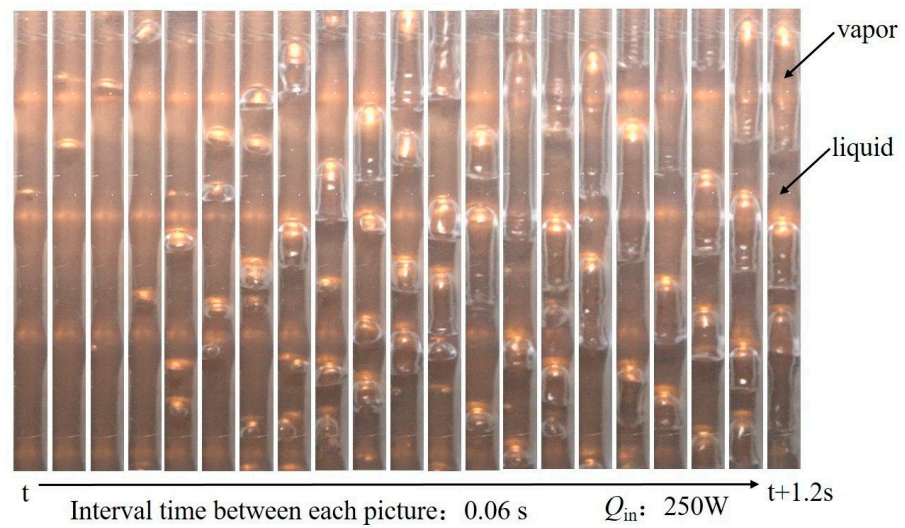
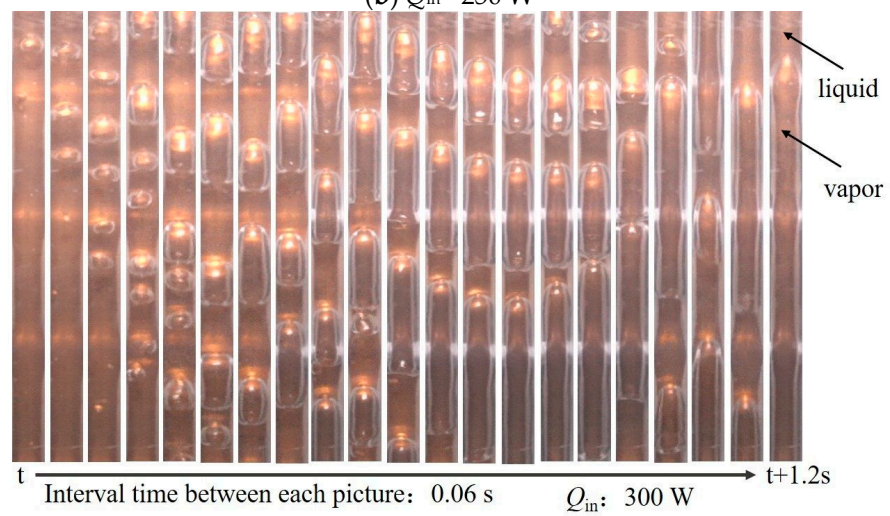
(a) $Q_{in} = 200\text{ W}$ (b) $Q_{in} = 250\text{ W}$ (c) $Q_{in} = 300\text{ W}$

Figure 5. Cont.

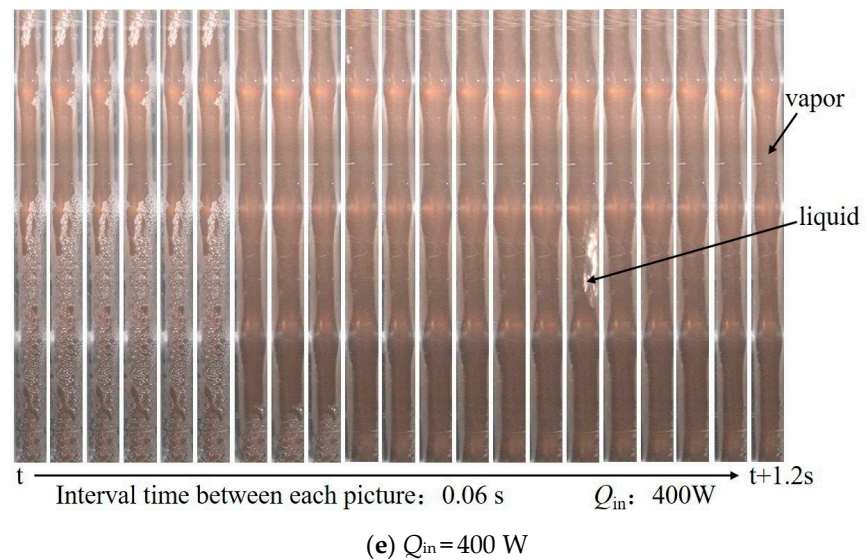
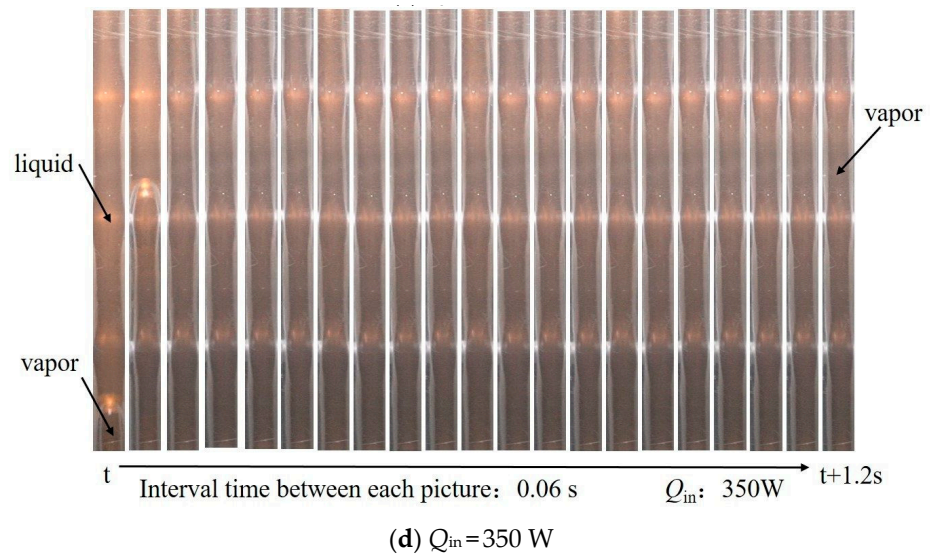


Figure 5. The boiling behavior of the working fluid in Window I under stable operation of an ultra-long gravity heat pipe at different heat input when the fill height is 6 m.

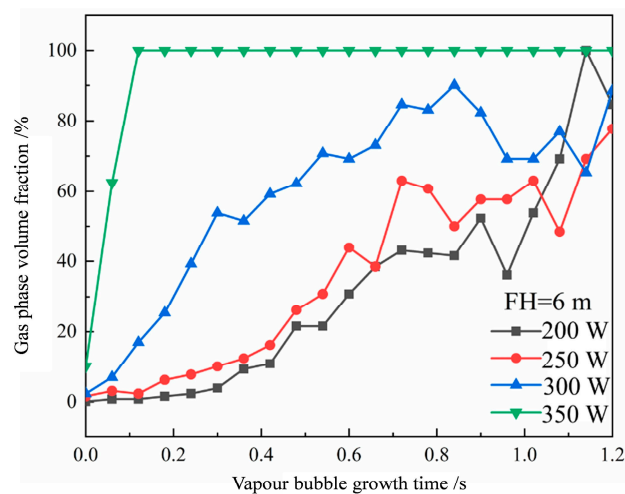


Figure 6. Variation of the volume fraction of the vapor phase in Window I with time during boiling of the working fluid at different heat input.

As shown in Figure 5a, under a heating power of 200 W, the working fluid produces nucleation and forms bubbles of roughly the same size as the tube diameter within approximately 0.36 s. Bubble flow was observed predominantly between 0.36s and 0.66s, progressing into slug flow as time increases with the bubbles moving upwards. As shown in Figure 6, for low heating levels (200 W and 250 W), the volumetric fraction of vapor grows relatively slowly during the initial formation of bubble. Within the first 0.36 s, the vapor volume fraction is less than 20%, representing the process of nucleation transitions into bubble flow. With the transition from bubble flow to slug flow, the vapor volume fraction enlarges to approximately 50%. It is noteworthy that the aforementioned nucleation does not persistently exist at low heating levels (200 W and 250 W). During long-term observation up to 600 s, in the case of 200 W heating power, only 7.5% of the time displayed significant vaporization nucleation and bubble growth behavior, while the remainder of time exhibited monophasic liquid without observing a gas–liquid interface. Similarly, in the case of 250 W heating power, a duration of approximately 40% was observed with single-phase liquids without any indication of a gas–liquid interface, indicating that the boiling phase transition of the liquid working fluid inside the tube segment is inadequacy.

When the heating power is 300 W, as shown in Figure 5c, once the vapor nucleus is formed, it immediately turns into a vapor bubble and rapidly forms a slug flow within 0.18 s. As shown in Figure 6, the vapor phase fraction increases rapidly, reaching 60% within the first 0.36 s, and then maintaining at around 80%. During a 600 s long observation period, significant vaporization nucleation and bubble growth behavior exist in about 81.7% of the Window I tube segment, indicating that the phase change rate of this tube segment is high and stable at this point.

Under heating power of 350 W, as shown in Figure 5d, the boiling of the working fluid in the tube is mainly composed of slug and annular flows. The liquid working fluid absorbs heat rapidly and forms a slug flow quickly, which lifts up the upper liquid working fluid. This lifting process causes the upper liquid working fluid to fall along the tube wall, leading to the formation of an annular flow. The volume fraction of the vapor phase in the Window I reaches 100% rapidly within 0.12 s and maintains for a long time. When the heating power continues to increase to 400 W, as shown in Figure 5e, it is observed that all the liquid in the upper part of Window I has evaporated, and the liquid pool level is below Window I. The liquid working fluid intermittently moves from top to bottom and wets the tube wall. Observations indicate that only about 4% of the time in the whole Window I tube segment is able to observe the condensed fluid moving down along the tube wall, and significant wetting exists at this time. For most of the remaining time, it may exist in the state of dry burning, indicating that severe dry burning problems exist in the lower part of the evaporating section of the heat pipe.

3.3. Two-Phase Flow Behavior in the Adiabatic Section

Figure 7 shows two-phase flow phenomena observed in sight Window II under the different heating powers (250 W, 300 W, 350 W). As shown in Figure 7a, at a heating power of 250 W, the condensate flows downwards intermittently, resembling a liquid beam annular circulation. The flow pattern inside the tube at 200 W is similar to that at 250 W. The upward moving steam carries the downward moving condensate with the steam taking the liquid near the center of the pipe to the wall, and then the condensate falls along the wall. Under this operating condition, there exists distinctive channel between the steam and condensate. As shown in Figure 7b, at a heating power of 300 W, the steam is found to condense, forming a liquid column with the characteristics of plug flow inside the adiabatic section. The liquid column moves from top to bottom and appears in sight Window II with an average interval of 14 min and 29 s, lasting about 3.45 s. During each interval between observations of the liquid column in sight Window II, the condensate forms intermittent liquid beam annular circulation, and there maintained respective flow channels between the upward moving steam and the downward moving condensate. With the heating power being increased to 350 W and 400 W, the condensate is observed to

form liquid beam annular circulation resembling the one shown in Figure 7c, and no liquid columns are recorded.

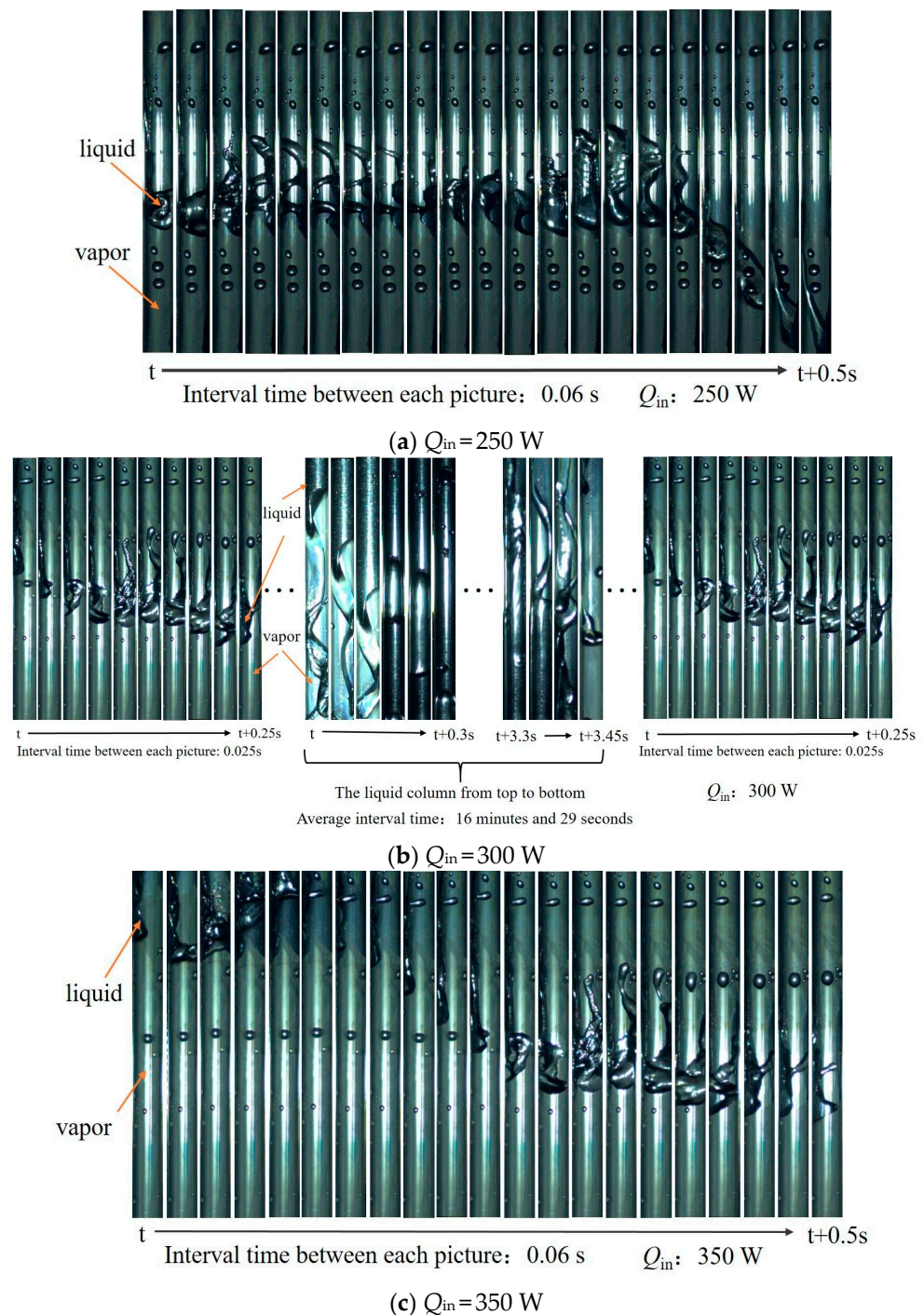
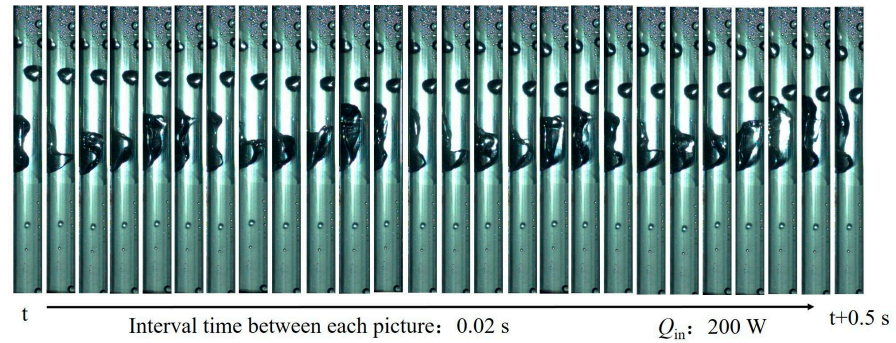


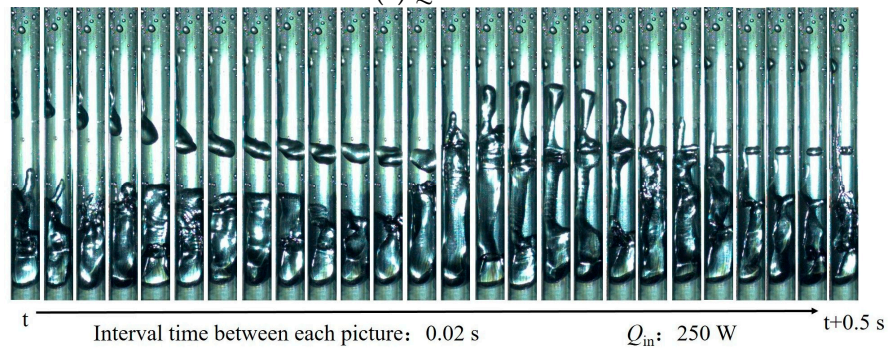
Figure 7. The two-phase flow behavior of the working fluid in Window II under stable operation of an ultra-long gravity heat pipe at different heating powers.

The stable operation of the extremely long gravity heat pipe in Window III is observed, and its two-phase flow behavior is displayed in Figure 8. As shown in Figure 8a, under a heat input of 200 W, the downward flowing condensate and upward moving vapor interacted to form intermittent liquid jet ring flows. With a heat input increase to 250 W, illustrated in Figure 8b, the condensate coalesced during its descent and the amount of condensate backflow markedly increased. Under the entrainment effect of upward moving

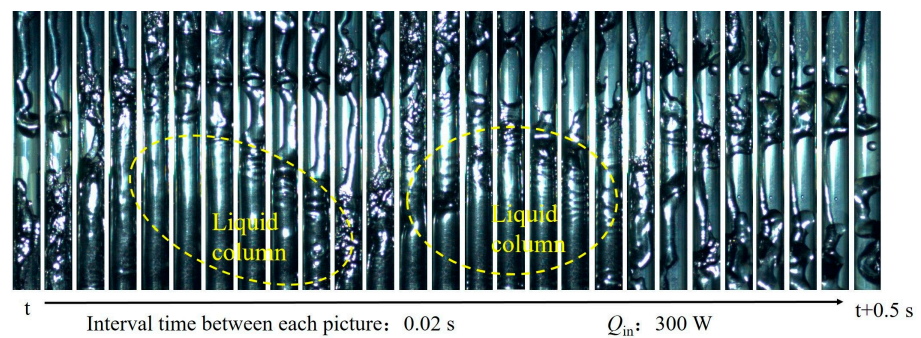
vapor, the intermittent formation of condensed lumps occurred, which were of the same size as the pipe diameter, but quickly dispersed into liquid jet flows. By incorporating the observations of the two-phase flow behavior at the entrance of the adiabatic section in Window II, it is evident that at low heat input (200 W, 250 W), ring-shaped liquid jet flows formed during the descent of the condensate, while there are separate flow paths for the back-flowing condensate and vapor moving in opposite directions.



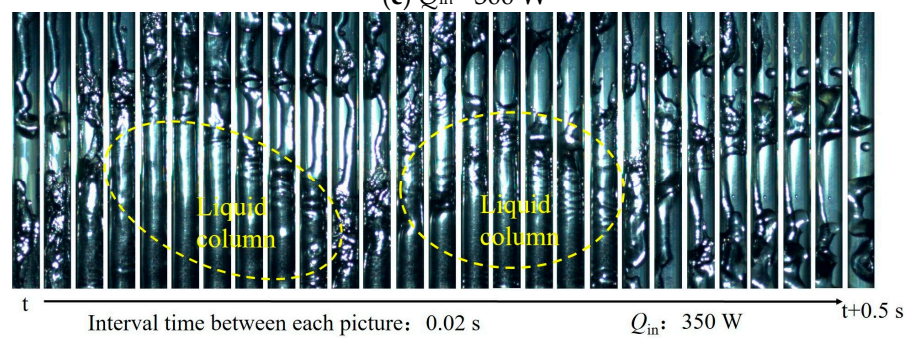
(a) Q_{in} = 200 W



(b) Q_{in} = 250 W



(c) Q_{in} = 300 W



(d) Q_{in} = 350 W

Figure 8. Cont.

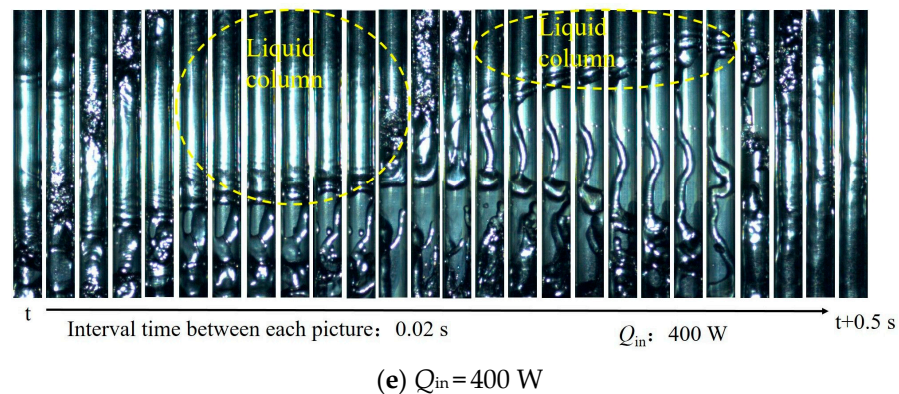


Figure 8. The two-phase flow behavior of the working fluid in window III under stable operation of an ultra-long gravity heat pipe at different heating powers.

Continuing to increase the heat input to 300 W, as shown in Figure 8c, a liquid column appears in Window III. The liquid column formed by the condensate completely filled the pipeline is lifted by the vapor to the upper half of Window III and begins to fall back, during which the upper part of the liquid column dispersed into liquid jet flows. The liquid column formed by the condensate lasted for about 0.38 s, accounting for roughly about 76% of the time during which it choked the pipeline. Most of the time, the liquid column stayed within Window III and the lower part of the viewport and did not enter the condensation section. When combined with the previously observed two-phase flow behavior at the entrance of the adiabatic section in Window II, it is evident that under a heat input of 300 W, the condensed backflow formed a liquid column in the lower part of viewport III, but the liquid column can flow back into the heating section.

As the heating power increased to 350 W, as shown in Figure 8d, a visible disparity emerged when compared with the case when the heat input is 300 W. Specifically, only the lower part of the liquid column at the interface of the phase was observed in Window III, indicating that a part of the liquid column formed in the adiabatic section had entered the condensation section. Due to the effect of the rising steam, the liquid column briefly falls back from the condensation section flowing back in the form of a stream into the adiabatic section. This action is quickly lifted and is followed by the lifting of the liquid back into the condensation section, an iterative phenomenon. Moreover, the liquid column formed by the condensate continued to exist.

When the heating input is 400 W, as shown in Figure 8e, the two-phase flow phenomenon in Window III is basically similar to that of 350 W. After the condensate forms the liquid column and enters the adiabatic section from the condensation section, it takes 2.64 s before the liquid column is observed to be lifted by the steam into the condensation section. At this point, the formed liquid column may be longer, and the liquid column moved back and forth between the adiabatic section and the condensation section. According to the velocity of the interface of the lower phase boundary of the liquid column in the figure, the length of the liquid column was roughly estimated to be around 1.5 m. By comparing the two-phase flow phenomena in Window II and Window III, it can be seen that at a higher heating power (350 W, 400 W), some liquid working fluid may stay for a long time in the upper part of the adiabatic section and the condensation section in the form of a long liquid column. This hinders the ascent of steam and significantly increases the temperature gradient near the exit of the adiabatic section of the heat pipe (area c in Figure 4). At the same time, only part of the condensate can form a liquid jet ring flow to flow back into the heating section. The trapped condensate in the upper part of the adiabatic section and the condensation section can limit the flow of condensate back to the heating section, failing to adequately wet the pipe wall, and resulting in a sharp temperature rise as depicted in area “b” of Figure 4.

3.4. Limitations on the Heat Transfer Performance of Ultra-Long Gravity Heat Pipe

Combining the observation results from various perspectives, it can be seen that when the heating power is less than 300 W, the heating section attains sufficient moisture content but a low evaporation rate (Figure 5a,b), while the gas–liquid backflow in the adiabatic section is smooth (Figures 7a and 8a,b). The primary factor that restricts the heat transfer performance of the heat pipe is the reduced evaporation rate of the working fluid in the heating section.

From the temperature data obtained in Figure 9, it can be seen that when the heat input is 200 W, the temperature of the pipe above 4.5 m is relatively uniform, while the temperature of the pipe below 4.5 m increases sharply. This indicates that the working fluid in the pipe section above 4.5 m should be in a saturated state of gas–liquid, and the liquid pool level should be around 4.5 m. The pressure of the liquid working fluid under the liquid pool can be determined using $P = P_{\text{sat}} + \rho_{\text{lg}}g\Delta h$, where P_{sat} is the vapor saturation pressure above the liquid pool, which can be calculated based on the average temperature of the heating section above the liquid pool. Δh is the distance between the liquid pool level and the position of the liquid working fluid. Similarly, when the heating power is 250 W, the height of the liquid pool should be around 4 m. The theoretical saturation temperature of the working fluid in the liquid pool for heating powers of 200 W and 250 W is shown in Figure 9. By comparing it with the experimental temperature data, it can be observed that the working fluid has not yet reached a steady-state boiling condition in the lowermost 3 m of the heat pipe under both heat inputs. Due to the fact that the bottom of the evaporator section remains mainly in a boiling suppression state most of the time, the liquid-phase working fluid absorbs heat mainly through sensible heat storage, after which it causes an abnormal temperature rise as shown in region “a” in Figure 4, increases the heat dissipation to the environment, and reduces the heat transfer rate of the heat pipe. Therefore, the boiling suppression caused by the high hydraulic head of the liquid pool in the lower part of the ultra-long gravity heat pipe evaporator section is the main reason that restricts the heat transfer efficiency of the heat pipe under low heating conditions.

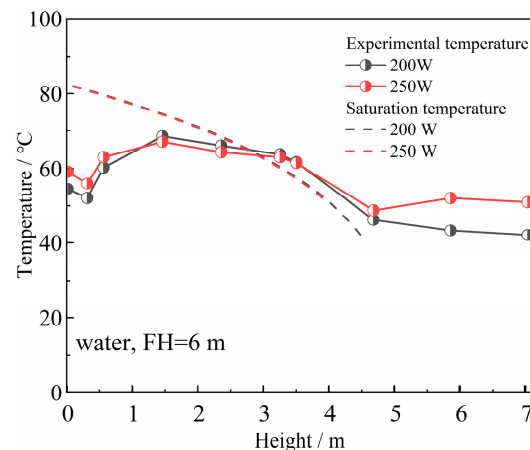


Figure 9. Comparison between the lower heating section’s temperature of the ultra-long gravity heat pipe and the corresponding saturation temperature when the fill height is 6 m and heat input is 200 W or 250 W.

The problems of boiling suppression caused by liquid accumulation gradually alleviate with the increase in the heating power. At a 300 W heating power, the evaporation rate in the heating section experiences a rapid increase and enters into a relatively stable evaporative phase change state (Figure 5c). At the same time, although liquid columns intermittently appear in the adiabatic sections, the path for steam rising and condensed liquid reflux is unobstructed, and there is no condenser liquid column blockage or heating section drying phenomenon (Figures 5c, 7b and 8c). This indicates that, although the gas–liquid co-flow causes certain fluid resistance, it has not yet seriously affected the steam condensation and

liquid evaporation. At this time, the temperature gradient of the full section of the heat pipe is small (as shown in Figure 4, $-0.6\text{ }^{\circ}\text{C}/\text{m}$), and the heat transfer performance of the heat pipe is improved, indicating better a heat transfer rate (Figure 3).

As the heating power increases to 350 W and 400 W, prolonged dryness is observed at the bottom of the heating section and it is dry for a long time (Figure 5e), while flow entrainment causes most of the condensed fluid in the adiabatic section to be carried away to the condensing section (Figure 8d,e). On the one hand, this hinders steam condensation in the condensing section and severely affects the heat transfer performance of the condensing section, resulting in the overcooling of the condensing section, as shown in the significant increase in the temperature gradient at the outlet of the adiabatic section in area c of Figure 4. On the other hand, a large amount of condensed fluid is trapped in the upper part of the adiabatic section, or even in the condensing section. The amount of liquid flowing back into the heating section is reduced, and the bottom of the heating section may be dried out (Figure 5e). As a result, the wall temperature of the pipe increases (area a in Figure 4), leading to the deterioration of the heat transfer performance of the heat pipe. Therefore, it can be seen that the blockage of liquid column in the condensing section caused by gas–liquid co-flow is the main reason that restricts the heat transfer.

4. Conclusions

In this paper, we have conducted visualization experiments to explore the heat transfer characteristics of the phase change flows in ultra-long gravity heat pipes with an injection height of 6 m (30% injection rate) and a heating power range from 200 to 400 W. The following conclusions can be drawn:

- (1) It is observed that the heat transfer capacity and heat transfer rate of the heat pipe increase firstly and then decrease with the increasing of the heating power. The optimal heat transfer performance was achieved at 162 W, with a heat transfer rate of 31%.
- (2) At low heating powers (200 W, 250 W), the heating section is well-wetted, but the evaporation rate is relatively low. The gas–liquid backflow in the adiabatic section is smooth. It is concluded that the main reason limiting the heat transfer performance of the heat pipe is the low evaporation rate of the working fluid in the heating section.
- (3) At a moderate heating power of 300 W, the evaporation rate in the heating section increases rapidly while remaining stable. Although liquid columns appear intermittently in the adiabatic section, the path of steam rising and condensate flowing back is unobstructed, and there is no blocking of condensate column in the condenser or drying phenomena in the heating section. Furthermore, even though the gas–liquid slugging causes certain counter-current resistance, it has not seriously affected steam condensation and reflux-evaporation. At this point, the temperature gradient along the heat pipe full length is small, leading to a better heat transfer efficiency and rate.
- (4) As the heating power continues to increase (350 W, 400 W), drying appears in the lower part of the heating section, and most of the condensate from the adiabatic section is carried to the condensation section by gas–liquid slugging. On the one hand, this hinders steam condensation in the condensation section, seriously affecting its heat transfer performance and resulting in sub-cooling. On the other hand, a large amount of condensate is trapped in the upper part of the adiabatic or even the condensation section, less liquid returns to the heating section causing the lower part of the heating section to be dry-out for a long time, the wall temperature of the heat pipe rises, and the heat transfer performance deteriorates. At this moment, the blockage of condensate column caused by the condensation of the gas–liquid mixture is the primary cause that restricts the heat transfer efficiency at a high heating power.

The visual experimental study in this paper has confirmed the different degradation mechanisms of heat transfer performance of ultra-long gravity heat pipes under low and high heating conditions. The research results may help guide the structural improvement of ultra-long gravity heat pipes and improve their heat transfer performance.

Author Contributions: Conceptualization, F.J.; methodology, J.C. (Juanwen Chen) and J.C. (Jiwen Cen); investigation, F.L., Q.M. and Z.L.; writing—original draft preparation, F.L. and W.H.; writing—review and editing, J.C. (Juanwen Chen); supervision and resources, F.J. All authors have read and agreed to the published version of the manuscript.

Funding: This research was funded by the National Key Research and Development Program (Grant No. 2021YFB1507301, 2021YFB1507300), Youth Science Fund (E52206126), Jiangyin Science and Technology Innovation Special Fund [Grant No. JY0604A021015210001PB], and Jiangsu Provincial Carbon Peak Carbon Neutralization Technology Innovation Special Fund [Grant No. BE2022012].

Data Availability Statement: The authors confirm that the data supporting the findings of this study are available within the article.

Conflicts of Interest: The authors declare that they have no known competing financial interests or personal relationships that could have appeared to influence the work reported in this paper.

Nomenclature

Q_{in}	heat input of the heat section/W
Q_{out}	heat output of the condenser section/W
ρ	density of coolant water/kg·m ⁻³
ρ_l	density of working fluid/kg·m ⁻³
c_p	isobaric heat capacity/J·kg ⁻¹ ·K ⁻¹
v_c	mass flow rate of the coolant water/m·s ⁻¹
P_{sat}	saturation temperature/K
T	temperature/K
Δh	distance from the liquid interface of the liquid pool/m
D	diameter/m

References

- Jiang, F.; Huang, W.; Cao, W. Mining Hot Dry Rock Geothermal Energy by Heat Pipe: Conceptual De-sign and Technical Feasibility Study. *Adv. New Renew. Energy* **2017**, *5*, 426–434.
- Huang, W.; Cao, W.; Jiang, F. A novel single-well geothermal system for hot dry rock geothermal energy exploitation. *Energy* **2018**, *162*, 630–644. [[CrossRef](#)]
- Huang, W.; Cen, J.; Chen, J.; Cao, W.; Li, Z.; Li, F.; Jiang, F. Heat extraction from hot dry rock by super-long gravity heat pipe: A field test. *Energy* **2022**, *247*, 123492. [[CrossRef](#)]
- Huang, W.; Chen, J.; Cen, J.; Cao, W.; Li, Z.; Li, F.; Jiang, F. Heat extraction from hot dry rock by super-long gravity heat pipe: Effect of key parameters. *Energy* **2022**, *248*, 123527. [[CrossRef](#)]
- Kusaba, S.; Suzuki, H.; Hirowatari, K.; Mochizuki, M.; Mashiko, K.; Nguyen, T.; Akbarzadeh, A. Extraction of geothermal energy and electric power generation using a large scale heat pipe. In Proceedings of the World Geothermal Congress, Kyushu-Tohoku, Japan, 28 May–10 June 2000; pp. 3489–3494.
- Liu, H.; Wang, X.; Zheng, L.; Yao, H.; Zhu, Y.; Wang, Y. Temperature response and thermal performance analysis of a super-long flexible thermosyphon for shallow geothermal utilization: Field test and numerical simulation. *Int. J. Heat Mass Transf.* **2022**, *192*, 122915. [[CrossRef](#)]
- Wang, X.; Yao, H.; Li, J.; Wang, Y.; Zhu, Y. Experimental and numerical investigation on heat transfer characteristics of ammonia ther-mosyphons at shallow geothermal temperature. *Int. J. Heat Mass Transf.* **2019**, *136*, 1147–1159. [[CrossRef](#)]
- Reay, D.A.; Kew, P.A.; Mcglen, R.J. Chapter 2—Heat Transfer and Fluid Flow Theory. In *Heat Pipes*, 6th ed.; Reay, D.A., Kew, P.A., Mcglen, R.J., Eds.; Butterworth-Heinemann: Oxford, UK, 2014; pp. 15–64.
- Wenbo, H.; Wenjong, C.; Tingliang, L.; Fangming, J. Numerical study and economic analysis of gravity heat pipe hot dry rock geothermal system. *CIESC J.* **2021**, *72*, 1302–1313.
- Moon, S.-H.; Park, Y.-W.; Yang, H.-M. A single unit cooling fins aluminum flat heat pipe for 100 W socket type COB LED lamp. *Appl. Therm. Eng.* **2017**, *126*, 1164–1169. [[CrossRef](#)]
- Tian, E.; He, Y.-L.; Tao, W.-Q. Research on a new type waste heat recovery gravity heat pipe exchanger. *Appl. Energy* **2017**, *188*, 586–594. [[CrossRef](#)]
- Wang, Y.; Wang, B.; Zhu, K.; Li, H.; He, W.; Liu, S. Energy saving potential of using heat pipes for CPU cooling. *Appl. Therm. Eng.* **2018**, *143*, 630–638. [[CrossRef](#)]
- Zeghari, K.; Louahia, H.; Le Masson, S. Experimental investigation of flat porous heat pipe for cooling TV box electronic chips. *Appl. Therm. Eng.* **2019**, *163*, 114267. [[CrossRef](#)]
- Zhang, M.; Lai, Y.; Zhang, J.; Sun, Z. Numerical study on cooling characteristics of two-phase closed thermosyphon embankment in permafrost regions. *Cold Reg. Sci. Technol.* **2011**, *65*, 203–210. [[CrossRef](#)]

15. Sbaity, A.A.; Louahlia, H.; Le Masson, S. Performance of a hybrid thermosiphon condenser for cooling a typical data center under various climatic constraints. *Appl. Therm. Eng.* **2022**, *202*, 117786. [[CrossRef](#)]
16. Jasim, A.K.; Freegah, B.; Alhamdo, M.H. Numerical and experimental investigation of a thermosiphon solar water heater system thermal performance used in domestic applications. *Heat Transf.* **2021**, *50*, 4575–4594. [[CrossRef](#)]
17. Ozbas, E. A novel design of passive cooler for PV with PCM and two-phase closed thermosyphons. *Sol. Energy* **2022**, *245*, 19–24. [[CrossRef](#)]
18. Tong, Z.; Fang, C.X.; Zang, G.J.; Wu, H. Experimental study on the passive regulation of a CO₂ two-phase thermosiphon loop. *Appl. Therm. Eng.* **2023**, *219*, 119457. [[CrossRef](#)]
19. Lin, T.; Quan, X.J.; Cheng, P. Experimental investigation of superlong two-phase closed thermosyphons for geothermal utilization. *Int. J. Therm. Sci.* **2022**, *171*, 107199. [[CrossRef](#)]
20. Hu, C.J.; Yu, D.L.; He, M.S.; Mei, H.P.; Yu, J.; Li, T.S. Performance evaluation of ultra-long lithium heat pipe using an improved lumped parameter model. *Nucl. Sci. Tech.* **2021**, *32*, 141. [[CrossRef](#)]
21. Tingliang, L.; Jiwen, C.; Wenbo, H.; Fangming, J. Experimental study on heat transfer performance of super long gravity heat pipe. *CIESC J.* **2020**, *71*, 997–1008.
22. Chen, J.; Cen, J.; Huang, W.; Jiang, F. Multiphase flow and heat transfer characteristics of an extra-long gravity-assisted heat pipe: An experimental study. *Int. J. Heat Mass Transf.* **2020**, *164*, 120564. [[CrossRef](#)]
23. Wang, X.; Liu, H.; Wang, Y.; Zhu, Y. CFD simulation of dynamic heat transfer behaviors in super-long thermosyphons for shallow geothermal application. *Appl. Therm. Eng.* **2020**, *174*, 115295. [[CrossRef](#)]
24. Wang, F.; Liu, X.; Jiang, B.; Zhuo, H.; Chen, W.; Chen, Y.; Li, X. Low-loading Pt nanoparticles combined with the atomically dispersed FeN₄ sites supported by FeSA-N-C for improved activity and stability towards oxygen reduction reaction/hydrogen evolution reaction in acid and alkaline media. *J. Colloid Interface Sci.* **2023**, *635*, 514–523. [[CrossRef](#)] [[PubMed](#)]
25. Li, Q.; Wang, F.; Wang, Y.; Zhou, C.; Chen, J.; Forson, K.; Miao, R.; Su, Y.; Zhang, J. Effect of reservoir characteristics and chemicals on filtration property of water-based drilling fluid in unconventional reservoir and mechanism disclosure. *Environ. Sci. Pollut. Res.* **2023**, *30*, 55034–55043. [[CrossRef](#)] [[PubMed](#)]
26. Li, Q.; Zhao, D.; Yin, J.; Zhou, X.; Li, Y.; Chi, P.; Han, Y.; Ansari, U.; Cheng, Y. Sediment Instability Caused by Gas Production from Hydrate-bearing Sediment in Northern South China Sea by Horizontal Wellbore: Evolution and Mechanism. *Nat. Resour. Res.* **2023**, 1–26. [[CrossRef](#)]
27. Sakamoto, Y.; Sato, T.; Kobayashi, H. Development study of a capacitance void fraction sensor using asymmetrical electrode plates. *J. Fluid Sci. Technol.* **2016**, *11*, JFST0008. [[CrossRef](#)]
28. Hewlin, R.L.; Kizito, J.P. Development of a Capacitance Based Void Fraction Sensor for Two-Phase Flow Measurements. In *Fluids Engineering Division Summer Meeting*; American Society of Mechanical Engineers: New York, NY, USA, 2013; Volume 55584, p. V002T11A005. [[CrossRef](#)]

Disclaimer/Publisher's Note: The statements, opinions and data contained in all publications are solely those of the individual author(s) and contributor(s) and not of MDPI and/or the editor(s). MDPI and/or the editor(s) disclaim responsibility for any injury to people or property resulting from any ideas, methods, instructions or products referred to in the content.